




## Key factors of stretch-flangeability of sheet materials

Jae Ik Yoon<sup>1</sup>, Jaimyun Jung<sup>1</sup>, Jung Gi Kim<sup>1</sup>, Seok Su Sohn<sup>2</sup>, Sunghak Lee<sup>1,2</sup>, and Hyoung Seop Kim<sup>1,2,3,\*</sup> 

<sup>1</sup>Department of Materials Science and Engineering, Pohang University of Science and Technology (POSTECH), Pohang 37673, Republic of Korea

<sup>2</sup>Center for Advanced Aerospace Materials, Pohang University of Science and Technology (POSTECH), Pohang 37673, Republic of Korea

<sup>3</sup>Center for High Entropy Alloys, Pohang University of Science and Technology (POSTECH), Pohang 37673, Republic of Korea

**Received:** 19 December 2016

**Accepted:** 15 March 2017

**Published online:**  
20 March 2017

© Springer Science+Business  
Media New York 2017

### ABSTRACT

Stretch-flangeability evaluated using hole-expansion testing represents the ability of sheet materials to resist edge fracture during complex shape forming. Despite a property imperative for automotive part applications of advanced high-strength steels, factors governing stretch-flangeability are not yet well understood. In this study, the mechanical properties of a selected group of materials with different microstructures were investigated using tensile, fracture toughness, and hole-expansion tests to find the factor governing the stretch-flangeability that is universally applicable to a variety of metallic materials. It was found that the fracture toughness of materials, measured using the fracture initiation energy, is a universal factor governing stretch-flangeability. We verified that fracture toughness is the key factor governing stretch-flangeability, showing that the hole-expansion ratio could be well predicted using finite element analysis associated with a simple ductile damage model, without explicitly taking into account the microstructural complexity of each specimen. This validates the use of the fracture toughness as a key factor of stretch-flangeability.

### Introduction

Currently, automotive industries are subjected to strong pressure to reduce exhaust emission of their automobiles, which is an important cause of air pollution. To address this imposition, automotive industries have focused on the development of a lightweight body-in-white using high-strength sheet steel. The development of lightweight automobile bodies has a variety of other goals as well, such as increasing fuel efficiency, increasing strength and

safety, and improving durability [1–4]. Advanced high-strength steels (AHSS) with excellent tensile properties such as dual phase (DP), transformation induced plasticity (TRIP), twinning induced plasticity (TWIP), quenching and partitioning (Q & P), and lightweight steels have been developed to meet these goals [5–11].

However, formability, which is the ability to be shaped into a desirable structure without fracture, becomes a problem in high-strength grade steels. Generally, the formability of these steels is

Address correspondence to E-mail: hskim@postech.ac.kr

insufficient compared with that of conventional low-strength grade sheet steels [12–14]. In particular, automotive parts that take advantage of complex forming processes are greatly challenged by the low formability of AHSS. Among different formability indices, stretch-flangeability of sheet materials (the ability to resist edge fracture during complex shape forming) is very poor in AHSS, when compared with conventional low-grade sheet steels. Indeed, the low stretch-flangeability of AHSS is an impediment to weight reduction of automotive parts [15–18].

Previous studies on sheet formability have mainly correlated tensile properties and sheet formability and focused on forming property analysis using forming limit diagrams (FLDs) and other numerical models during the forming process [19–26]. While it is possible to predict a success or failure of sheet forming under appointed conditions with high accuracy [27–29], edge fracture during the edge-stretch process cannot be accurately predicted using previous models, which employ FLD and tensile properties in the finite element method (FEM) [15, 30, 31]. Thus, stretch-flangeability has become a particularly important, yet not well understood, sheet forming property. This makes it hard to predict the edge-stretch forming process and to develop AHSS having excellent stretch-flangeability. Therefore, understanding the factors that govern stretch-flangeability has become important for improving stretch-flangeability for automotive applications of AHSS sheets.

There were previous studies for investigating the deformation behavior and governing factors of stretch-flangeability, which is indicated by the hole-expansion ratio (HER) measured with a hole-expansion test (HET) [32]. The deformation behavior during the HET was reported to be similar to that of uniaxial tensile deformation [33]. Thus, the correlations between the tensile properties and HER of specific steel groups were reported [33–43]. Nonetheless, because these correlations were limited to specific steels, the results were conflicting. In addition, the relationships between the microstructural features of materials and the HER were also investigated in previous studies, but the results indicated that the influences of microstructure were only limited to similar steel grades [16, 17, 42, 43]. Therefore, in order to clearly understand the factor governing stretch-flangeability, a variety of factors as well as deformation behavior and microstructural features should be taken into account.

In previous studies, factors other than deformation behavior and microstructural features that affect stretch-flangeability of sheet materials have been reported. It should be noted that the HER of the same material strongly depends upon the initial hole processing methods and edge surface condition of the HET specimen. According to the ISO/TS 16630 standard procedure for evaluating HER [32], the initial central hole of a HET specimen should be manufactured using a punching process, which inevitably generates an accumulated shearing damage and initial defects such as micro-voids and micro-cracks. These initial defects act as crack initiation sites [16, 41, 42, 44, 45]. Consequently, the evaluation of stretch-flangeability involves the analysis of material behavior with many initial defects and accumulated shear damage. However, conventional formability measurements, such as drawability and stretchability, are based on evaluation of intrinsic material properties. Therefore, fracture behavior of materials having initial defects, as well as intrinsic material properties, should be taken into account in evaluation of stretch-flangeability. In previous research conducted by the authors, the correlation between fracture toughness and HER of AHSS having various microstructures and tensile properties was investigated [44].

In this study, we extend the evaluation window to include diverse materials ranging from AHSS and low-strength steel to nonferrous material sheets, thus covering various microstructures and mechanical properties. Through this, we verify that fracture toughness is a universal factor governing stretch-flangeability. Also, for cross-validation of the key factor of stretch-flangeability, finite element analysis (FEA) is performed using a simple ductile damage model.

## Materials and experimental procedure

### Materials

In this study, eight different materials were used. The materials were selected to represent different tensile properties and microstructures. The AHSS samples (Steel A–D) were fabricated in POSCO, and the low-strength grade steels and nonferrous materials were commercial products (purity of pure Cu: 99.99%). All the specimens were cold-rolled (CR) except for the

**Table 1** Grain size and phase of various sheet specimens

Specimens information	Steel A	Steel B	Steel C	Steel D	AZ31	Pure Cu	HR IF	CR IF
Phase	$\alpha + \alpha'$	$\alpha + \alpha'$	$\alpha + B + \gamma$	$\alpha + \gamma$	$\alpha - \text{Mg} + \text{few } \beta$	Cu	$\alpha$	$\alpha$
Average grain size ( $\mu\text{m}$ )	$d_{\text{BCC}} = 2.73$	$d_{\text{BCC}} = 5.64$	$d_{\text{BCC}} = 4.74$ $d_{\gamma} = 0.96$	$d_{\alpha} = 6.11$ $d_{\gamma} = 0.85$	$d_{\text{Mg}} = 8.55$	$d_{\text{Cu}} = 37.32$	$d_{\alpha} = 51.26$	$d_{\alpha} = 41.49$

$\alpha$ : ferrite,  $\gamma$ : austenite,  $\alpha'$ :  $\alpha'$ -martensite,  $\beta$ :  $\text{Mg}_{17}\text{Al}_{12}$  B: bainite

hot-rolled (HR) IF steel. The pure Cu was fully annealed at 600 °C for 2 h in the Ar gas atmosphere before the tests. The average grain size and phases are summarized in Table 1.

### Mechanical testing

Uniaxial tensile tests were carried out using a servo-hydraulic universal testing machine (UTM, model 1361, Instron Co., USA) to determine the tensile properties of the sheet specimens at room temperature (298 K). The tensile tests were conducted according to the ASTM E8/E8M standard procedure [46] with dog-bone-shaped plate specimens of 5.0 mm gauge length, 2.5 mm gauge width, and 1.0 mm thickness, at a strain rate of 0.001 s<sup>-1</sup>. Three specimens were tested in three different directions (0°, 45°, and 90°) with respect to the rolling direction (RD). The strain-hardening exponent value ( $n$  value) was considered at the true strain where necking onsets under uniaxial tension [47]. The normal anisotropy value ( $\bar{R}$  value) was calculated using the following equation [48]:

$$\bar{R} = \frac{R_0 + 2R_{45} + R_{90}}{4}, \quad (1)$$

where  $R_0$ ,  $R_{45}$ , and  $R_{90}$  are the plastic strain ratios of each loading direction. During the tensile tests, the strains were measured using the digital image correlation (DIC) method in an optical strain gauge system (ARAMIS 5 M, GOM mbH, Germany) [49].

The strain rate sensitivity (SRS) value ( $m$  value) was measured using a strain rate jump test in RD at different strain rates (0.01 and 0.001 s<sup>-1</sup>). The strain rate jump tests were conducted using the sample dimension identical to that used in the uniaxial tensile test. The SRS value was calculated from the true stress-strain curves using the following equation [47]:

$$m = \frac{\ln(\sigma_2/\sigma_1)}{\ln(\dot{\epsilon}_2/\dot{\epsilon}_1)}, \quad (2)$$

where  $\sigma_1$  and  $\sigma_2$  are true stresses at true strain rates  $\dot{\epsilon}_1$  and  $\dot{\epsilon}_2$ , respectively, at a certain strain.

Fracture toughness tests were conducted according to the ASTM E1820 standard procedure except for the specimen dimension [50]. While ASTM E1820 requires the specimen thickness to be large enough for a plane strain condition, the sheet sample's thickness in this study could not satisfy the test conditions. The fracture toughness tests were performed at a strain rate of 0.001 s<sup>-1</sup> using a single-edge-notched tensile (SENT) specimen of 60.0 mm total length, 15.0 mm width, 1.0 mm thickness, and 3.0 mm initial sharp notch in the RD, machined by electric discharge machining. The SENT specimens were prepared so that total crack lengths (notch length + fatigue crack length) were 0.4–0.5 times the specimen width. Fatigue cracks were introduced under tension at the frequency of 10 Hz sinusoidal cyclic loading, between 8 and 39% of the yield strength (YS) (stress ratio = 0.2) of the specimen. ASTM E1820 recommends the evaluation of the minimum specimen thickness for a size-independent value of fracture toughness, using the following equation [50]:

$$B = 10 \frac{J_Q}{\sigma_Y}, \quad (3)$$

where  $B$  is the specimen thickness and  $\sigma_Y$  is the effective yield strength ( $\sigma_Y = \sigma_{YS} + \sigma_{UTS}/2$ ). However, in this study, because the eight different materials had a wide range of YS, UTS, and limitation of initial sample thickness, it was hard to directly compare the fracture toughness of different specimens using  $J_c$  or  $K_{Ic}$  under a non-plane strain condition. This point will be discussed in detail in a later section. Thus, for comparing the ability of a material containing a crack to resist fracture, we defined the fracture initiation energy ( $E_i$ ) as equivalent to that used in Charpy impact testing. Figure 1 shows the defined area of fracture initiation energy. During the

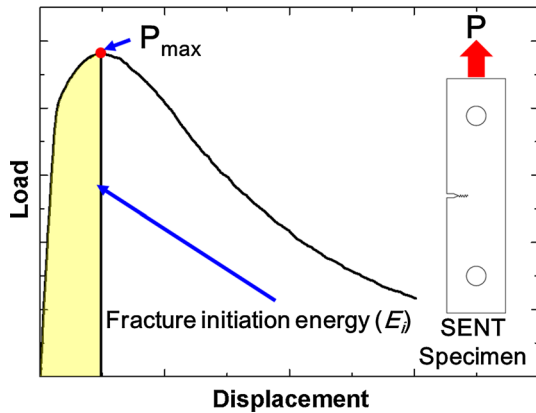


**Figure 1** Schematic diagram of load–displacement curve in fracture toughness test. The filled area before the  $P_{max}$  defines the fracture initiation energy ( $E_i$ ).

fracture toughness tests, the displacement was also measured using the DIC method.

The HETs were performed using an Erichsen hydraulic universal sheet metal testing machine (model 145-60, Erichsen Co., Germany) with a 60° conical punch to measure the HER of each specimen. According to the ISO/TS 16630 standard procedure [32], 90.0 × 90.0 mm<sup>2</sup> square specimens with 10.0 mm diameter initial central hole and 1 mm thickness were used in this test. The initial central hole was made using a punching process, with a punch with a diameter of 10.1 mm and a die with an inside diameter of 10.2 mm. The punching clearance was 5.0%. The HETs were conducted at a constant punch speed of 10 mm/min with a constant blank holder force of 200 kN, to prevent slipping of the specimen. The tests were stopped when the main crack of the hole-edge region propagated along the thickness direction. The final hole diameters were measured after the tests. The HER was calculated using the following equation [32]:

$$HER (\%) = \frac{d_f - d_0}{d_0} \times 100, \tag{4}$$

where  $d_0$  and  $d_f$  are initial and final hole diameters, respectively. In this study, the HER was decided as an average value after three tests of each specimen.

### Microstructure characterization

Microstructural features, such as the phase and the average grain size, of each material were investigated using field emission scanning electron microscopy

(FE-SEM, XL-30S FEG, Philips Co., Netherlands) equipped with electron backscatter diffraction (EBSD). The EBSD scan on the FE-SEM was operated at 25 kV. The EBSD data were post-processed using the orientation imaging microscopy (OIM) analysis software (TSL OIM analysis 5.2, EDAX Inc., USA). EBSD specimens of the steel samples were mechanically polished and then electro-polished in a solution of 8% perchloric acid (60%) + 92% acetic acid (99.5%) by volume fraction at an operating voltage from 40 to 70 V, depending on the specimens. EBSD specimens of pure Cu and AZ31 were prepared using mechanical polishing and then final polishing using 0.04 μm colloidal silica suspension.

### Finite element analysis

To verify the governing factor and deformation behavior of stretch-flangeability, three-dimensional static elasto-plastic FEM simulations were conducted in an engineering workstation using the commercial FEM package ABAQUS version 6.9. Specimen dimensions for the fracture toughness test simulations were the same as those for the experimental fracture toughness tests. Also, the dimensions of the HET simulation, such as specimen dimension, the form of the conical punch, and test die shapes, were the same as those used in the experimental HET setups. In the HET simulation, the features of the punched hole surface such as roll over zone and burnished zone were not taken into account, and its effect will be discussed later. For the HET simulation, more than 10,000 8 node, fully integrated hexahedral elements (C3D8) were used and more elements were used near the hole. The damage model parameters obtained from fitting the load displacement curves of fracture toughness simulations to those of the experiments were used. The schematic diagram of the conical HET tools and mesh discretization of HET simulation is shown in Fig. 2.

The focus of the present work lies in quantifying the key mechanical property that governs the HER of various sheet materials. While initially hole-punched specimens may not contain sharp-notched crack initiation sites that are present in fracture toughness specimens, the punched specimen’s surface has micro-voids and small defects that act as stress concentration sites, leading to fracture. Judging from the fact that specimens with clear hole-edge surfaces exhibited a large increase in HER compared with those with defective hole-edge surfaces [16, 51], one

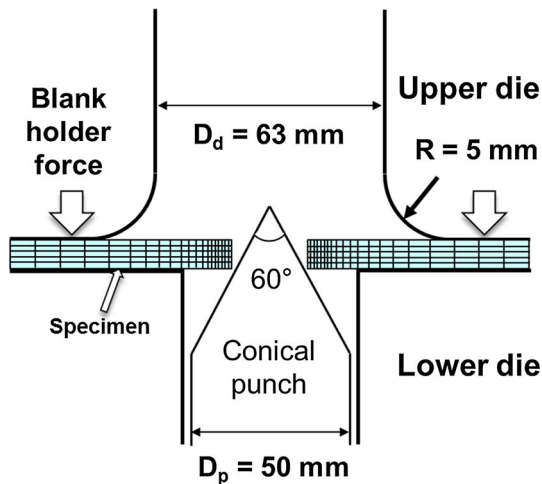


**Figure 2** Schematic diagram of the conical HET tools and mesh discretization of HET simulation.

could expect the micro-voids and defects to act as crack initiation sites. Thus, the qualitative similarity between crack initiation sites due to micro-voids and defects, and those due to sharp-notched cracks (which is quantified by fracture toughness), infers a clear relation between HER and fracture toughness.

The anisotropy of each specimen was captured using the quadratic yield function proposed by Hill [52]:

$$f = \frac{1}{\sqrt{F(\sigma_{22} - \sigma_{33})^2 + G(\sigma_{33} - \sigma_{11})^2 + H(\sigma_{11} - \sigma_{22})^2 + 2L\sigma_{23}^2 + 2M\sigma_{31}^2 + 2N\sigma_{12}^2}} \quad (5)$$

where the  $f$  is equivalent stress for Hill's yield criterion and the parameters  $F$ ,  $G$ ,  $H$ ,  $L$ ,  $M$ , and  $N$  are defined as follows:

$$F = 0.5 \left( \frac{1}{R_{22}^2} + \frac{1}{R_{33}^2} - \frac{1}{R_{11}^2} \right) \quad (6)$$

$$G = 0.5 \left( \frac{1}{R_{33}^2} + \frac{1}{R_{11}^2} - \frac{1}{R_{22}^2} \right) \quad (7)$$

$$H = 0.5 \left( \frac{1}{R_{11}^2} + \frac{1}{R_{22}^2} - \frac{1}{R_{33}^2} \right) \quad (8)$$

$$L = 0.5 \left( \frac{3}{R_{23}^2} \right) \quad (9)$$

$$M = 0.5 \left( \frac{3}{R_{13}^2} \right) \quad (10)$$

$$N = 0.5 \left( \frac{3}{R_{12}^2} \right), \quad (11)$$

where the  $R_{ij}$  can be calculated from the experimentally obtained Lankford's  $r$  values [53].

$$R_{11} = R_{13} = R_{23} = 1 \quad (12)$$

$$R_{22} = \sqrt{\frac{R_{90}(R_0 + 1)}{R_0(R_0 + 1)}} \quad (13)$$

$$R_{33} = \sqrt{\frac{R_{90}(R_0 + 1)}{(R_0 + R_{90})}} \quad (14)$$

$$R_{12} = \sqrt{\frac{3(R_0 + 1)R_{90}}{(2R_{45} + 1)(R_0 + R_{90})}} \quad (15)$$

Lankford's  $r$  values of the specimens are summarized in Table 2. The fully annealed pure Cu was assumed to be an isotropic material ( $\bar{R}$  value = 1.00).

A simple ductile damage model was used to simulate the load–displacement curve of each specimen during the fracture toughness test. The fracture toughness test simulations were conducted with C3D8 hexagonal elements. More than 40,000 elements were used with a bias near the crack tip where the elements retained a characteristic length of 0.01–0.15 mm, which is within the range of element sizes typically used for ductile failure modeling [54–56]. Larger sized elements were used for IF steels and Cu, with or without damage model, to avoid a steep drop in load bearing capacity due to strain localization before reaching the maximum load values.

The ductile damage model first requires a damage onset strain ( $\epsilon_D^{pl}$ ) and a damage indicator ( $w_D$ ). The damage indicator is defined as follows:

**Table 2** Experimental results of Lankford's  $r$  values of the specimens

Lankford's $r$ values	Steel A	Steel B	Steel C	Steel D	AZ31	Pure Cu	HR IF	CR IF
$R_0$	0.74	0.63	0.74	0.51	1.77	–	1.52	1.84
$R_{45}$	0.96	0.98	0.90	0.79	2.15	–	1.04	1.33
$R_{90}$	0.95	0.80	0.97	0.67	2.98	–	1.36	2.09

$$w_D = \int \frac{d\bar{\epsilon}^{pl}}{\epsilon_D^{pl}}, \tag{16}$$

where damage starts when  $w_D = 1$  and the equivalent plastic strain is defined as follows [53]:

$$d\bar{\epsilon}^{pl} = \sqrt{\frac{F(d\epsilon_{11}^{pl})^2 + G(d\epsilon_{22}^{pl})^2 + H(d\epsilon_{33}^{pl})^2}{FG + FH + GH} + \frac{2(d\epsilon_{23}^{pl})^2}{L} + \frac{2(d\epsilon_{31}^{pl})^2}{M} + \frac{2(d\epsilon_{12}^{pl})^2}{N}}, \tag{17}$$

Once the damage starts, the material softens until its stiffness ( $E$ ) degrades to ‘0,’ that is, when the material fractures. After the onset of damage, a damage variable  $D$  will represent the degradation of the material stiffness. With increasing  $D$ , the load bearing capacity of the initially undamaged materials ( $\sigma$ ) will resort to  $(1-D)\sigma$  with stiffness ( $E$ ) degrading to  $(1-D)E$ , assuming a linear relation between material stiffness and damage variable. Once  $D$  of an element reaches the value of 1, the element is eliminated. Linear softening behavior was assumed in describing the evolution of the damage variable. In this assumption, the damage variable increases according to Eq. (18) [53].

$$\dot{D} = \frac{L\dot{\epsilon}^{pl}}{w_f^{pl}} \quad \text{if } p \leq 0, \tag{18}$$

where  $L$ ,  $\dot{\epsilon}^{pl}$ , and  $p$  are characteristic element length, plastic strain rate, and pressure, respectively.  $w_f^{pl}$  is the equivalent plastic displacement at failure, which is computed as

$$w_f^{pl} = 2G_f/\sigma_y, \tag{19}$$

where  $G_f$  and  $\sigma_y$  are fracture energy per unit area and equivalent stress at the time the failure criterion is met (damage onset strain), respectively. The plastic dissipation from damage initiation to material fracture is used as input for linear softening behavior. Hill’s yield criterion was used to define the plastic flow of each specimen.

In modeling the damage behavior, the strain at which damage initiates ( $\epsilon_D^{pl}$ ) and the fracture energy ( $G_f$ ), or the energy required from the onset of the damage to complete fracture, need to be determined. This is accomplished by comparing the experimentally observed load–displacement curve with the simulated one, without any damage criteria up to the fracture initiation point, which is the maximum load

point in the experiment curve. The first appearance of discrepancy between the two curves signifies the onset of damage, and the strain value of the elements in front of the crack tip is used as  $\epsilon_D^{pl}$ .

Because  $G_f$  for model input is the fracture energy for single element, the fracture energy density should be determined. Direct assessment of the fracture energy is possible by simply finding the area below the experimental curve after identifying the damage initiation point assuming that crack initiates at the maximum load point. However, in order to calculate the fracture energy for each element, the fracture energy needs to be divided by all the elements that contribute to load bearing capacity. On the other hand, if the fracture energy is indirectly addressed by the difference between the areas under the curves, which is the energy loss due to the evolution of the damage variable, only the elements that are damaged need to be evaluated. Thus, the number of elements with accumulated plastic strain above  $\epsilon_D^{pl}$  was calculated, and the volume of the damaged region was estimated by adding up the characteristic volume of each element ( $V_{el}$ ) multiplied by its respective normalized strain value ( $\epsilon^{pl}/\epsilon_{max}^{pl}$ ). Afterward, the energy loss is divided by the volume of the damaged region to calculate the energy density lost due to damage, and total plastic dissipation energy density after damage onset is subtracted by the calculated energy density lost due to damage to determine  $G_f$ . Of course, the unit of the fracture energy is fracture energy per unit area, so the characteristic length of the element is multiplied before input.

Because the micro-voids and defects that cause changes in deformation mode are not individually resolvable at FEM scale, the fracture strain is assumed to be independent of stress triaxiality. This assumption entails that the damage evolution of finite elements in front of the crack tip will be identical to the damage evolution of the finite elements of the hole-edge surface of the punched specimen.

## Results and discussion

### Microstructural features

Figure 3 shows various microstructures of the sheet specimens. The average grain size and phases are summarized in Table 1. To find the factor governing

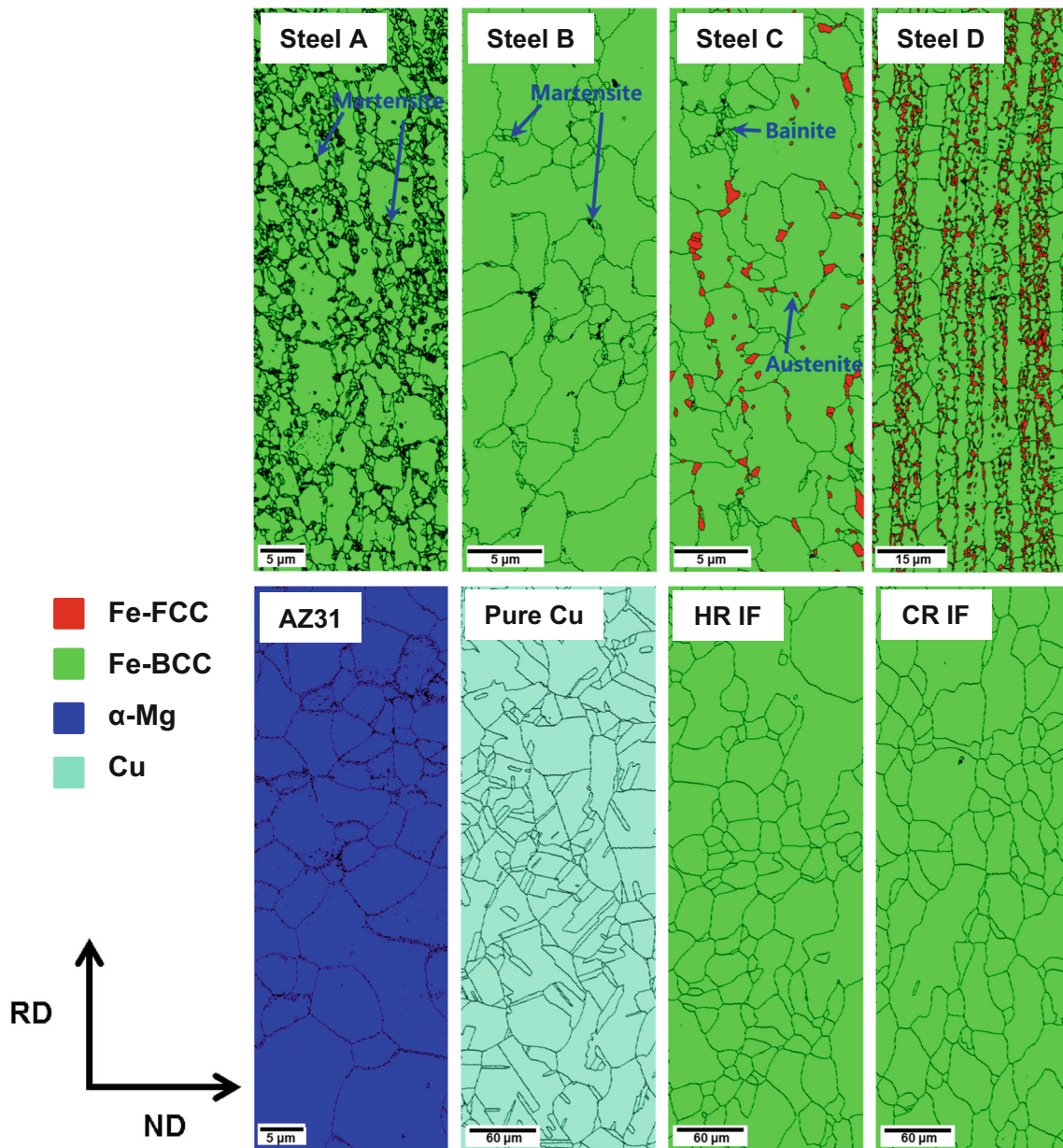


**Figure 3** EBSD phase maps of diverse testing specimens (for interpretation of the references to *color* in this figure, the reader is referred to the Web version of this article).

stretch-flangeability over a wide range of microstructures, we selected eight different materials with different microstructural features. For ferrous materials, two different IF steels, which were the ferrite single phase having different rolling conditions and grain sizes, were chosen. In addition, Steel A and Steel B with different martensite volume fractions and ferrite grain sizes, Steel C with a complex phase (e.g., ferrite, retained austenite, and bainite), and Steel D with ferrite matrix and austenite band structure were investigated. For nonferrous

materials, pure Cu with coarse grains and initial annealing twins and AZ31 magnesium alloy with a hexagonal close packed (HCP) structure were chosen for examination. Stretch-flangeability can be fundamentally understood by analyzing materials with various microstructural features.

### Stretch-flangeability

Figure 4 exhibits the strain and stress triaxiality trends in the hole-edge region during the HET as a

function of HER. The outer region (i.e., fracture initiation site) experiences a tensile-strain-dominant state during the HET. The stress triaxiality of the outer region was close to 0.35, meaning that the stress state was similar to the stress state during uniaxial tensile testing [57]. Thus, the deformation behavior during the HET can be defined as a tension-like deformation. Of course, during the early stage of deformation (HER < 20%), the stress triaxiality of the inner hole-edge region is negative. This means that the inner part of the hole-edge region is under compressive deformation because of the contact between the punch and the specimen. However, the initial compressive deformation of the inner region does not affect the overall fracture behavior because the fracture initiation sites during the HET are located in the outer region, and the deformation behavior in this region is tension like. Furthermore, the middle and inner regions also exhibited tension-like deformation at HER > 20%, where most of the materials fractured.

The HET results of the eight different materials are summarized in Table 3. Some of the mechanical properties of AHSS were already published in a previous study [44]. Although HET results have deviations because the values rely on the eyes of operators to observe crack initiation and propagation

along the thickness direction, these deviations did not affect the overall tendency. Thus, the HER values with a standard deviation were used in analyzing the factors governing the stretch-flangeability of materials. The various sheet materials tested in this study had a wide range of HER values from very low (AZ31: 10.1%) to very high (CR IF: 176.4%). By investigating these materials, we were able to propose factors governing stretch-flangeability that could not have been included using materials with limited range of HER. The mechanical properties of materials that control the stretch-flangeability will be discussed in the next section.

### Tensile properties

Figure 5 shows tensile engineering stress–strain curves and tensile true stress–strain curves along the RD of various specimens. Tensile tests of each specimen were performed three times, and the test results exhibit good reproducibility. Tensile properties of the specimens are summarized in Table 3, and Lankford’s *r* values of the specimens are summarized in Table 2. The fully annealed pure Cu was assumed to be an isotropic material ( $\bar{R}$  value = 1.00). The analysis of these specimens involved a wide range of

**Figure 4** During the HET simulation: **a** the strain and **b** stress triaxiality trend in the hole-edge region according to HERs for CR IF steel.

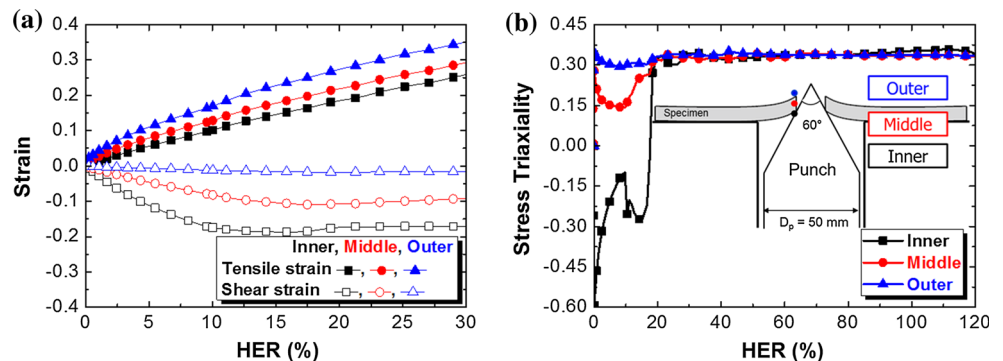
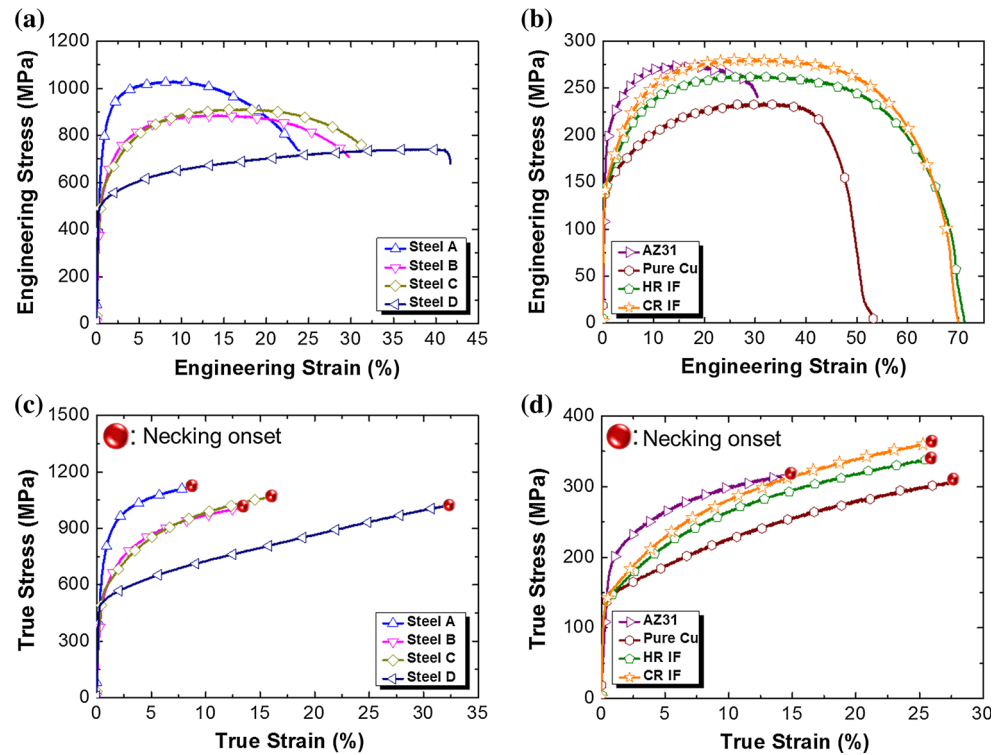


**Table 3** Tensile properties, fracture initiation energy, and HER of each specimen

Specimens	YS (MPa)	UTS (MPa)	U.EL (%)	T.EL (%)	PEL (%)	<i>n</i> value	<i>m</i> value	$\bar{R}$	$E_i$	HER (%)
Steel A	694 ± 29	1021 ± 12	9.2 ± 0.3	24.0 ± 0.4	14.8 ± 0.1	0.09	0.0064 ± 0.0012	0.90	1.12 ± 0.18	30.0 ± 2.4
Steel B	500 ± 10	884 ± 5	13.5 ± 0.7	29.7 ± 0.6	16.2 ± 1.2	0.13	0.0055 ± 0.0011	0.85	0.97 ± 0.12	27.9 ± 0.5
Steel C	521 ± 9	909 ± 6	16.7 ± 0.7	31.4 ± 0.2	14.7 ± 0.8	0.15	0.0044 ± 0.0005	0.88	0.77 ± 0.05	24.0 ± 1.5
Steel D	504 ± 7	724 ± 16	36.5 ± 1.9	42.8 ± 2.1	6.3 ± 2.3	0.31	0.0043 ± 0.0004	0.69	0.36 ± 0.10	16.3 ± 0.9
AZ31	182 ± 5	275 ± 1	14.9 ± 1.5	30.5 ± 1.7	15.5 ± 1.0	0.14	0.0127 ± 0.0027	2.26	0.21 ± 0.01	10.1 ± 0.2
Pure Cu	136 ± 3	232 ± 2	32.5 ± 1.5	53.8 ± 1.1	21.3 ± 2.3	0.28	0.0042 ± 0.0004	1.00	2.93 ± 0.54	92.2 ± 3.4
HR IF	134 ± 1	265 ± 2	29.6 ± 0.1	71.9 ± 1.0	42.3 ± 0.9	0.26	0.0179 ± 0.0015	1.24	2.57 ± 0.42	81.7 ± 8.9
CR IF	135 ± 10	290 ± 7	27.0 ± 0.4	66.6 ± 3.0	39.6 ± 3.3	0.24	0.0095 ± 0.0009	1.65	4.90 ± 0.20	176.4 ± 5.9



**Figure 5** a, b Tensile engineering stress–strain curves and c, d tensile true stress–strain curves of a, c AHSS, and b, d low-strength steels and nonferrous materials with respect to rolling direction.



tensile properties (e.g., YS, ultimate tensile strength (UTS), uniform elongation (U.EL), total elongation (T.EL), post-uniform elongation (P.EL),  $n$  value,  $m$  value, and  $\bar{R}$  value). If the tensile properties and HER of sheet materials are correlated, a universal trend should be observed between HER and each tensile property of the sheet materials.

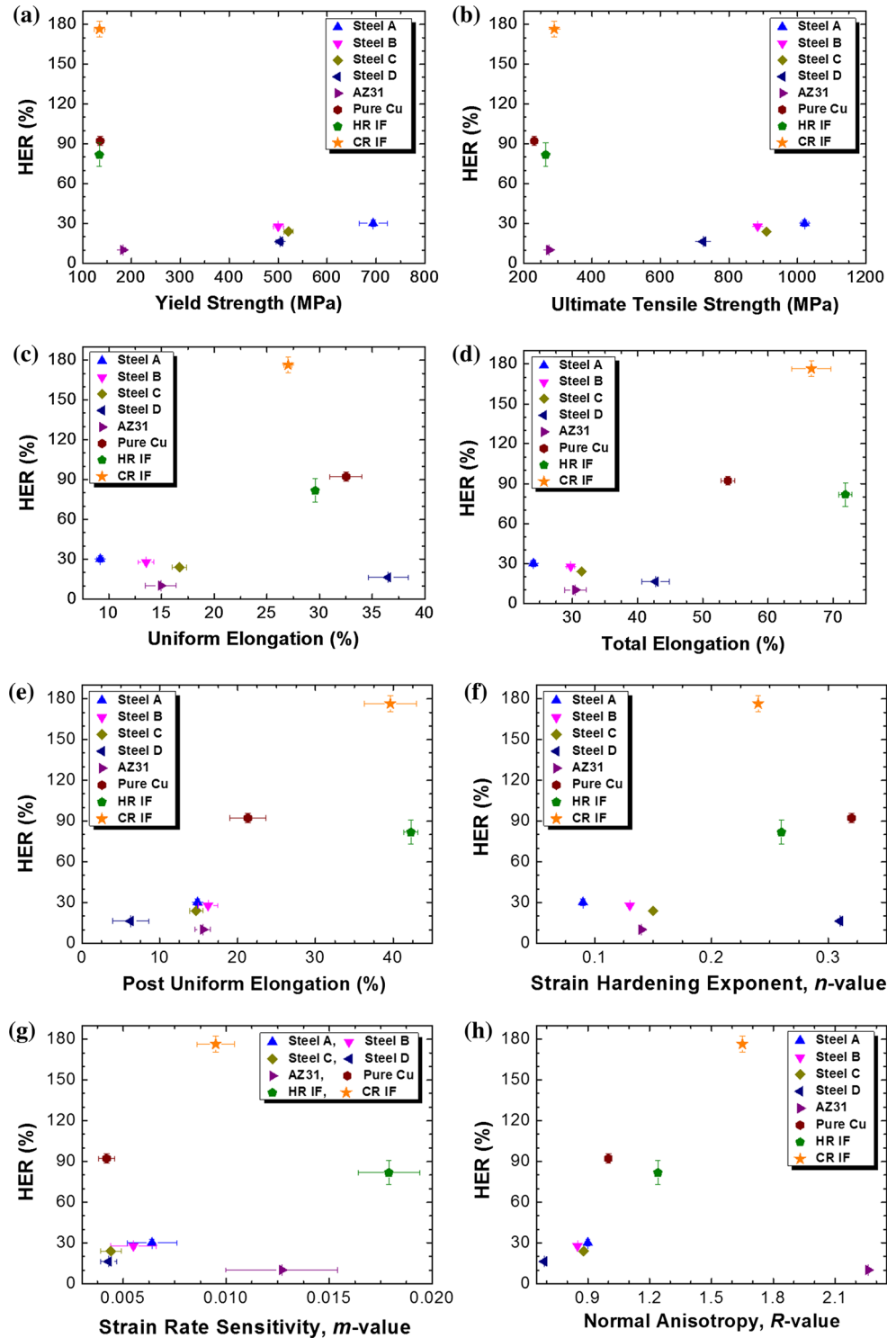
Figure 6 demonstrates the correlation between individual tensile property and HER of materials. Deformation behavior during the HET is similar to the uniaxial tensile deformation behavior; however, individual tensile properties are not correlated with the HER of various materials. This result supports the report that correlations between HER and tensile properties in previous studies are only valid for specific steel groups having similar microstructure or strength grade. Thus, these correlations cannot be generalized. It is especially important to note that the  $n$  value,  $m$  value, and  $R$  value, which are considered governing factors during various forming processes (e.g., deep drawing, and stretch forming [21, 22, 24]), do not seem to affect the HER of materials. This demonstrates that the key factors affecting stretch-flangeability are different from those affecting conventional formability. Moreover, Lee et al. [16] and Yoon et al. [51] reported that the HER of the same

material strongly relied on the initial hole processing methods and the edge surface status of the HET sample. In particular, removing the initial defects of the hole-edge region using the milling process notably improved the HERs. Therefore, this point should be considered for an accurate understanding of stretch-flangeability, and we should investigate not only deformation behavior during the stretch-flanging processing, but also other extrinsic factors that may affect stretch-flangeability.

### Stretch-flangeability from the fracture mechanics point of view

Figure 7 is an example of the initial hole-edge region of the HET specimen made using the punching process and it shows that many defects were generated in the initial hole-edge region during the punching process [44], when following the ISO/TS 16630 standard procedure. A few defects were observed in a burnished zone shown in Fig. 7c, and many defects (e.g., micro-voids and shearing dimples) were observed in a fracture zone shown in Fig. 7d, e. This result is in good agreement with the previous reports of hole-edge region observations. These defects act as strong crack initiation sites and significantly affect

**Figure 6** Correlations between individual tensile property and HER of specimens.



the HER of materials [16, 41, 42, 44, 45]. In fact, even in the same materials, the HER considerably increases if the process for making the initial hole is changed or the defects are removed in the hole-edge region before the HET [16, 51]. Therefore, it is almost

impossible to relate the HER to uniaxial tensile properties even if the stress state in the hole-edge region is similar to that in the tension region because stretch-flangeability of materials is evaluated using specimens with many initial defects and accumulated

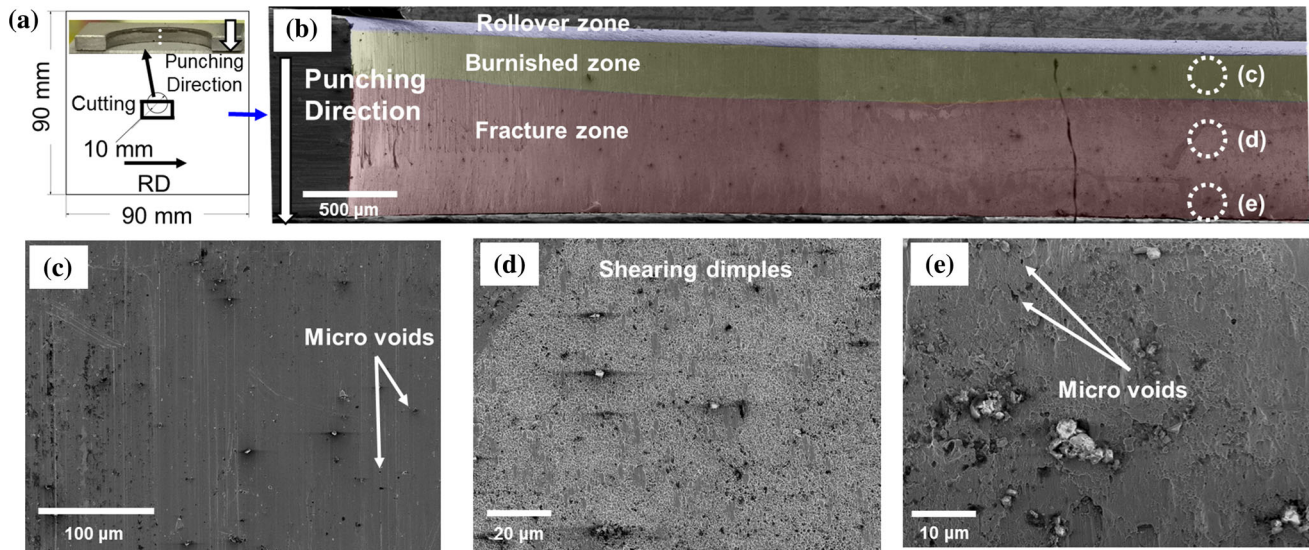


**Figure 7** SEM micrographs of the initial hole-edge region of the HET specimen made using a punching process [44]. The defects (e.g., micro-cracks and micro-voids) act as a strong crack initiation

site during the HET. *c* is *inner*, *d* is *middle*, and *e* is *outer* region in Fig. 4, respectively.

shear damage. This constitutes a primary difference between HET for stretch-flangeability and the other sheet formability tests such as deep drawability, stretchability, and bendability testing. Consequently, for an accurate understanding of stretch-flangeability, the fracture resistance of a material containing initial defects should be taken into account.

Fracture toughness can well represent the fracture resistance of materials having initial defects. If the fracture resistance of materials containing initial defects is an important factor in stretch-flangeability, the HER can be correlated with the fracture toughness of materials. In this study, fracture toughness tests were performed according to the ASTM E1820 standard procedure. However, the fracture toughness of sheet materials was evaluated using the fracture initiation energy instead of the conventional fracture toughness index,  $J_c$  or  $K_{Jc}$ , because these sheet materials were too thin. It should be noted that  $J_c$  or  $K_{Jc}$  depends upon the sample thickness. If the specimen is not thick enough to satisfy the plane strain condition,  $J_c$  or  $K_{Jc}$  is overestimated. Also, according to Eq. (3), the standard thickness for satisfying the plane strain condition is quite different for each material. Although specimens with a wide range of YS and UTS might have the same thickness, the deformation conditions would be different. For example, a material with a high YS and UTS (e.g.,

Steel A) satisfies the plane strain condition even with a thickness of only 3 mm, but a material with a low YS and UTS (e.g., pure Cu) must be thicker to satisfy the plane strain condition. Thus, in materials with a wide range of YS and UTS,  $J_c$  or  $K_{Jc}$  cannot be based upon the same evaluation standard even for specimens of the same thickness. Therefore, to compare the resistance of materials containing a crack to fracture, we defined fracture initiation energy ( $E_i$ ), equivalent to that used in Charpy impact testing. Note that the ductile materials, such as pure Cu, HR IF, and CR IF, were not easy to identify the maximum load in the fracture toughness tests, which is a critical factor for the definition of the fracture initiation energy. In this case, the maximum load point should be carefully chosen while tracking the load value in the load–displacement curves at fracture toughness tests.

Figure 8 indicates the correlation between the fracture toughness evaluated using fracture initiation energy, and the stretch-flangeability evaluated using HER. In this figure, as the fracture initiation energy of materials increases, HER increases linearly because of the similarity in the deformation mechanics between fracture toughness and HER. In other words, in the materials with higher fracture initiation energy, more energy is required to initiate a crack in the hole-edge region during the HET. Thus, we know that fracture

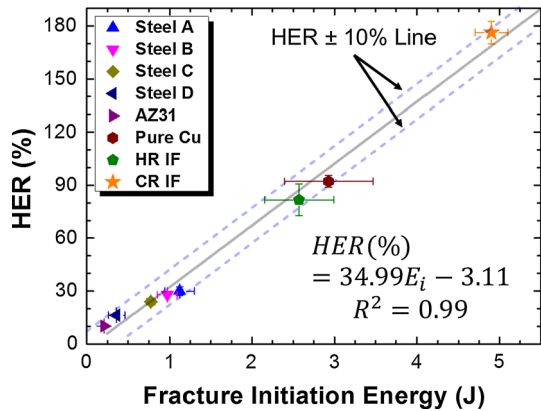


**Figure 8** Correlation between fracture initiation energy and HER of various specimens.

toughness is a key factor affecting the stretch-flangeability of materials.

### Finite element analysis of fracture toughness and hole-expansion test

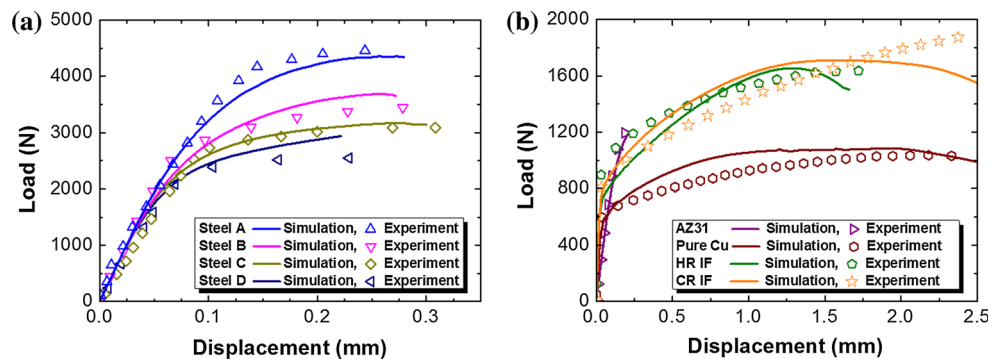
The simulated load–displacement curves in the fracture toughness tests in Fig. 9 are in good agreement with the experimental results. Figure 10 shows the FEA and experimental results in the hole-edge region of a specimen at the moment of failure. During the HET simulations, the failure moments were chosen so that all the elements along the thickness direction of the hole-edge region were deleted due to the accumulated damage there. The comparison of the HERs in Table 4 indicates that both the simulated HER values and the trend are in good agreement with the experimental results, verifying the hypothesis of this work. One can see that while the simu-

lated results based on the ductile damage model were overestimated, the overall results were well matched. Likely, the overestimations stem from the fact that direct transfer of parameters from the ductile damage model disregards the effect of the shear damaged zone, condition of the damaged surface, and the distribution of micro-voids and defects, which would have occurred during an actual punching process.

The size and morphology of the shear damaged zone differ from microstructure to microstructure, indicating that identical hole-punching processes manifest different damage or defect distributions for different materials. Hasegawa et al. [42] reported the shape of shear damaged zones and the morphology of micro-defects of AHSS sheets. The shape of initial defects and initial strain of HET specimens are not identical compared with a fracture toughness specimen with extremely sharp notch created by fatigue cracks. In addition, the distributions of micro-voids and defects should alter the local triaxiality during the HET, but the simulation assumed that fractures were triaxiality independent so that the damage evolution due to formation of a sharp notch during a fracture toughness test would be identical to the damage evolution of the hole-edge surface during the HET.

Nevertheless, the difference between the experimentally observed and predicted HERs was roughly 10% at best, and the trend in how specimens of high fracture toughness exhibit high HER is well reproduced. This indicates the validity of our approach in identifying fracture toughness as a key parameter of the HER of specimens with punched holes, without explicitly taking into account the microstructural complexity of each specimen [58].

**Figure 9** Comparison between experimental and fitted load–displacement curves for the fracture toughness tests of **a** AHSS and **b** other materials.



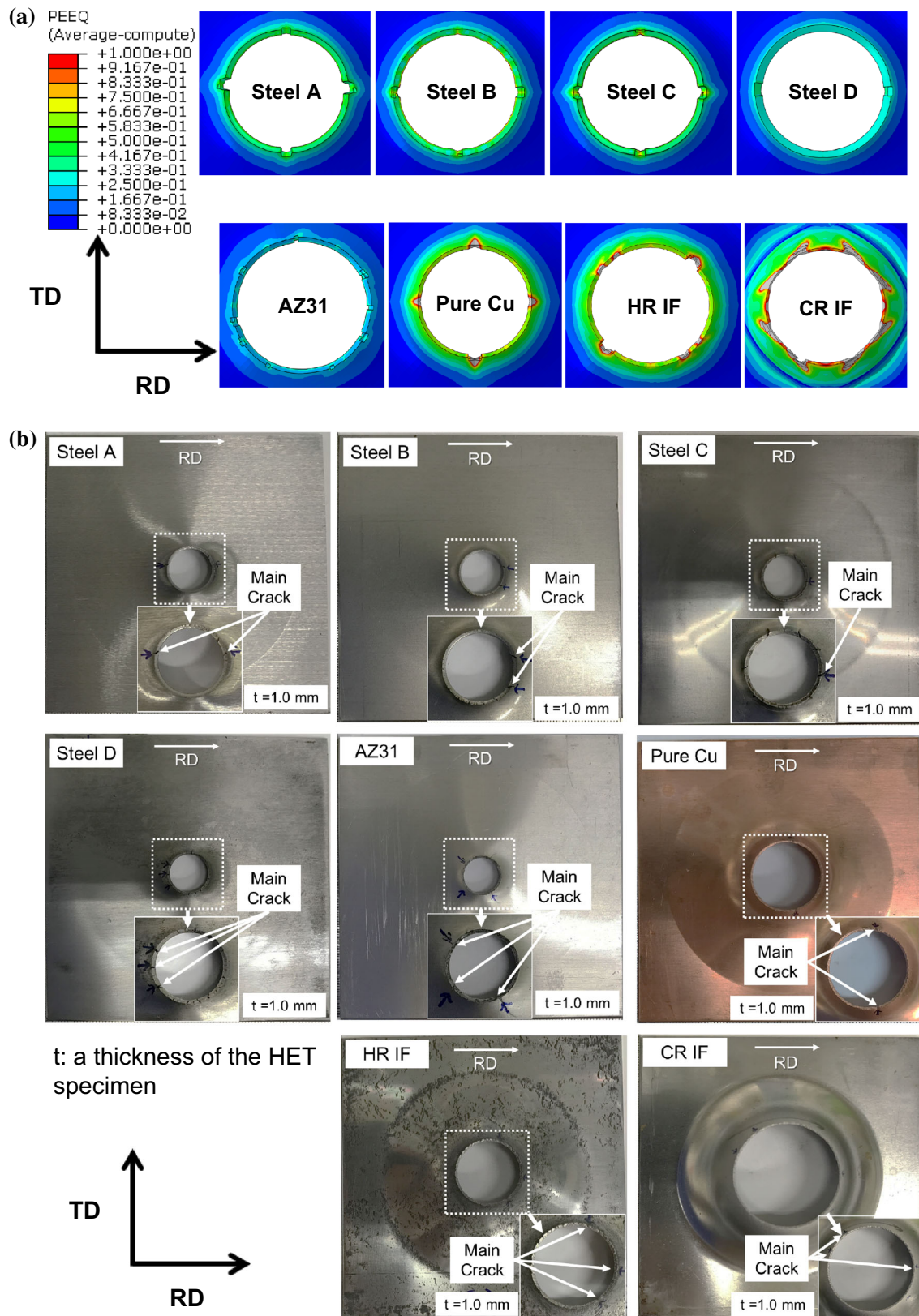


**Figure 10** a HET simulation and b experimental results at the moment of failure of each specimen.

**Table 4** Experimental and simulation results on the HER of each specimen

HER (%)	Steel A	Steel B	Steel C	Steel D	AZ31	Pure Cu	HR IF	CR IF
Experiment	30.0	27.9	24.0	16.3	10.1	92.2	81.7	176.4
Simulation	38.8	38.3	34.0	23.4	20.0	96.2	84.1	195.8

## Conclusions

In summary, to find a universal factor governing the stretch-flangeability of sheet materials, we investigated a variety of materials with different microstructures and mechanical properties. The following conclusions were obtained.

1. During the HET, the deformation behavior in the hole-edge region where the failure took place is comparable with that related to uniaxial tension. However, individual tensile properties are not correlated with the HER of various materials.
2. The HER of the same material considerably increases if the process for making the initial hole is changed or the defects are removed in the hole-edge region before the HET. Therefore, it is extremely difficult to directly correlate HER to uniaxial tensile properties without considering the condition of the hole-edge region.
3. Many defects are generated in the initial hole-edge region during the punching process when following the ISO/TS 16630 standard procedure. These defects act as strong crack initiation sites and significantly affect the HER of materials. That is, the stretch-flangeability of materials is evaluated using specimens with many initial defects. Therefore, the fracture resistance of material containing initial defects should be accounted for when evaluating stretch-flangeability.
4. The fracture toughness, measured using the fracture initiation energy, is a universal factor governing stretch-flangeability. This was verified by comparing the stretch-flangeability and mechanical properties of a variety of materials having different microstructural features and initial processing conditions. Also, HERs can be successfully predicted using a ductile damage model in FEA without explicitly taking into account the microstructural complexity of each specimen. This signifies the validity of our approach in identifying fracture toughness as a key factor of stretch-flangeability.
5. From the above results, development of the next generation AHSS with excellent stretch-flangeability should take into account its fracture toughness.

## Acknowledgement

This work was supported by the National Research Foundation of Korea (NRF) Grant funded by the Korea government (MSIP) (No. 2014R1A2A1A10051322).

## Compliance with ethical standards

**Conflict of interest** The authors declare that they have no conflict of interest.

## References

- [1] Mayyas A, Qattawi A, Omar M, Shan D (2012) Design for sustainability in automotive industry: a comprehensive review. *Renew Sustain Energy Rev* 16:1845–1862
- [2] Kuziak R, Kawalla R, Waengler S (2008) Advanced high strength steels for automotive industry. *Arch Civ Mech Eng* 8:103–117
- [3] Kwon O, Lee K, Kim G, Chin K-G (2010) New trends in advanced high strength steel developments for automotive application. *Mater Sci Forum* 638–642:136–141
- [4] Ma M, Yi H (2011) Lightweight car body and application of high strength steels. In: Weng Y, Dong H, Gan Y (eds) *Advanced Steels*, 1st edn. Springer, Berlin Heidelberg, pp 187–198
- [5] Fonstein N (2015) *Advanced high strength sheet steels: physical metallurgy, design, processing, and properties*, 1st edn. Springer, Switzerland
- [6] Tasan CC, Diehl M, Yan D, Bechtold M, Roters F, Schemmann L, Zheng C, Peranio N, Ponge D, Koyama M, Tsuzaki K, Raabe D (2015) An overview of dual-phase steels: advances in microstructure-oriented processing and micromechanically guided design. *Annu Rev Mater Res* 45:391–431

- [7] Alharbi F, Gazder AA, Kostryzhev A, De cooman BC, Pereloma EV (2014) The effect of processing parameters on the microstructure and mechanical properties of low-Si transformation-induced plasticity steels. *J Mater Sci* 49:2960–2974. doi:[10.1007/s10853-013-8008-z](https://doi.org/10.1007/s10853-013-8008-z)
- [8] Mandal G, Ghosh SK, Mukherjee S (2016) Phase transformation and mechanical behaviour of thermo-mechanically controlled processed high-strength multiphase steel. *J Mater Sci* 51:6569–6582. doi:[10.1007/s10853-016-9852-4](https://doi.org/10.1007/s10853-016-9852-4)
- [9] Sohn SS, Choi K, Kwak J-H, Kim NJ, Lee S (2014) Novel ferrite–austenite duplex lightweight steel with 77% ductility by transformation induced plasticity and twinning induced plasticity mechanisms. *Acta Mater* 78:181–189
- [10] Sohn SS, Song H, Suh B-C, Kwak J-H, Lee B-J, Kim NJ, Lee S (2015) Novel ultra-high-strength (ferrite + austenite) duplex lightweight steels achieved by fine dislocation substructures (Taylor lattices), grain refinement, and partial recrystallization. *Acta Mater* 96:301–310
- [11] Zargaran A, Kim HS, Kwak JH, Kim NJ (2015) Effect of C content on the microstructure and tensile properties of lightweight ferritic Fe-8Al-5Mn-0.1 Nb alloy. *Met Mater Int* 21:79–84
- [12] Jha G, Das S, Lodh A, Haldar A (2012) Development of hot rolled steel sheet with 600 MPa UTS for automotive wheel application. *Mater Sci Eng A* 552:457–463
- [13] Jha G, Das S, Sinha S, Lodh A, Haldar A (2013) Design and development of precipitate strengthened advanced high strength steel for automotive application. *Mater Sci Eng A* 561:394–402
- [14] Gerstein G, Besserer H-B, Nürnberger F, Barrales-Mora LA, Shvindlerman LS, Estrin Y, Maier HJ (2017) Formation and growth of voids in dual-phase steel at microscale and nanoscale levels. *J Mater Sci* 52:4234–4243. doi:[10.1007/s10853-016-0678-x](https://doi.org/10.1007/s10853-016-0678-x)
- [15] Chen M, Zhou DJ (2008) AHSS Forming simulation for shear fracture and edge cracking, great designs in steel seminar, autosteel, [www.autosteel.org](http://www.autosteel.org)
- [16] Lee J, Lee S-J, De Cooman BC (2012) Effect of microalloying elements on the stretch-flangeability of dual phase steel. *Mater Sci Eng A* 536:231–238
- [17] Lee J, Lee M, Do H, Kim S, Kang N (2014) Effect of the tempered martensite matrix and granular bainite on stretch-flangeability for 980 MPa hot-rolled steel. *Korean J Met Mater* 52:113–121
- [18] Kamibayashi K, Tanabe Y, Takemoto Y, Shimizu I, Senuma T (2012) Influence of Ti and Nb on the strength-ductility-hole expansion ratio balance of hot-rolled low-carbon high-strength steel sheets. *ISIJ Int* 52:151–157
- [19] Sing WM, Rao KP (1995) Influence of material properties on sheet metal formability limits. *J Mater Process Tech* 48:35–41
- [20] Sing WM, Rao KP (1997) Role of strain-hardening laws in the prediction of forming limit curves. *J Mater Process Tech* 63:105–110
- [21] Kang DH, Kim DW, Kim S, Bae GT, Kim KH, Kim NJ (2009) Relationship between stretch formability and work-hardening capacity of twin-roll cast Mg alloys at room temperature. *Scripta Mater* 61:768–771
- [22] Narayanasamy R, Ponalagusamy R, Raghuraman S (2008) The effect of strain rate sensitivity on theoretical prediction of limiting draw ratio for cylindrical cup drawing process. *Mater Des* 29:884–890
- [23] Zhang C, Leotoing L, Guines D, Ragneau E (2009) Theoretical and numerical study of strain rate influence on AA5083 formability. *J Mater Process Tech* 209:3849–3858
- [24] Yi S, Bohlen J, Heinemann F, Letzig D (2010) Mechanical anisotropy and deep drawing behaviour of AZ31 and ZE10 magnesium alloy sheets. *Acta Mater* 58:592–605
- [25] Evans M (2008) Measuring the predictive accuracy of various models of formability of Corus Tubular Blanks. *J Mater Sci* 43:2562–2573. doi:[10.1007/s10853-008-2472-x](https://doi.org/10.1007/s10853-008-2472-x)
- [26] Fathi H, Emadoddin E, Mohammadian Semnani HR, Mohammad Sadeghi B (2016) Effect of punch speed on the formability behavior of austenitic stainless steel type 304L. *Met Mater Int* 22:397–406
- [27] Chung K, Kim H, Lee C (2014) Forming limit criterion for ductile anisotropic sheets as a material property and its deformation path insensitivity part I: deformation path insensitive formula based on theoretical models. *Int J Plast* 58:3–34
- [28] Chung K, Lee C, Kim H (2014) Forming limit criterion for ductile anisotropic sheets as a material property and its deformation path insensitivity part II: boundary value problems. *Int J Plast* 58:35–65
- [29] Mekonen MN, Steglich D, Bohlen J, Stutz L, Letzig D, Mosler J (2013) Experimental and numerical investigation of Mg alloy sheet formability. *Mater Sci Eng A* 586:204–214
- [30] Ishiwatari A, Masaki U, Inazumi T (2013) Press forming analysis contributing to the expansion of high strength steel sheet applications, JFE Technical Report
- [31] Ye C, Chen J, Xia C, Yu X (2016) Study of curvature and pre-damage effects on the edge stretchability of advanced high strength steel based on a new simulation model. *Int J Mater Form* 9:269–276
- [32] ISO (2009) Metallic Materials—Method of Hole Expanding Test, International Organization for Standardization, <http://www.iso.org>
- [33] Paul SK (2014) Non-linear correlation between uniaxial tensile properties and shear-edge hole expansion ratio. *J Mater Eng Perform* 23:3610–3619

- [34] Adamczyk RD, Michal GM (1986) Sheared edge extension of high-strength cold-rolled steels. *J Appl Metalwork* 4:157–163
- [35] Chen L, Kim J-K, Kim S-K, Kim G-S, Chin K-G, De Cooman BC (2010) Stretch-flangeability of high Mn TWIP steel. *Steel Res Int* 81:552–568
- [36] Chatterjee S, Bhadeshia HKDH (2007) Stretch-flangeability of strong multiphase steels. *Mater Sci Technol* 23:606–609
- [37] Chen X, Jiang H, Cui Z, Lian C, Lu C (2014) Hole expansion characteristics of ultra high strength steels. *Procedia Eng* 81:718–723
- [38] Fang X, Fan Z, Ralph B, Evans P, Underhill R (2003) The relationships between tensile properties and hole expansion property of C-Mn steels. *J Mater Sci* 38:3877–3882. doi:10.1023/A:1025913123832
- [39] Xu L, Barlat F, Lee M-G (2012) Hole expansion of twinning-induced plasticity steel. *Scripta Mater* 66:1012–1017
- [40] Chun E-J, Lee J-S, Do H, Kim S-J, Choi Y-S, Park Y-H, Kang N (2012) Effects of coiling temperature and carbides behavior on stretch-flangeability for 980 MPa hot-rolled steels. *Korean J Met Mater* 50:487–493
- [41] Sirinakorn T, Uthaisangsk V, Srimanosaowapak S (2014) Effects of the tempering on mechanical properties of dual phase steels. *J Met Mater Miner* 24:13–20
- [42] Hasegawa K, Kawamura K, Urabe T, Hosoya Y (2004) Effects of microstructure on stretch-flange-formability of 980 MPa grade cold-rolled ultra high strength steel sheets. *ISIJ Int* 44:603–609
- [43] Cho Y-R, Chung J-H, Ku H-H, Kim I-B (1999) Effect of controlled cooling on the formability of TS 590 MPa grade hot-rolled high strength steels. *Met Mater Int* 5:571–578
- [44] Yoon JI, Jung J, Joo S-H, Song TJ, Chin K-G, Seo MH, Kim S-J, Lee S, Kim HS (2016) Correlation between fracture toughness and stretch-flangeability of advanced high strength steels. *Mater Lett* 180:322–326
- [45] Karelova A, Krempaszky C, Werner E, Tsipouridis P, Hebesberger T, Pichler A (2009) Hole expansion of dual-phase and complex-phase AHS steels—effect of edge conditions. *Steel Res Int* 80:71–77
- [46] ASTM (2015) Standard test methods for tension testing of metallic materials, ASTM International, [www.astm.org](http://www.astm.org)
- [47] Dieter GE, Bacon D (1988) *Mechanical Metallurgy*, SI Metric edn. McGraw-Hill, New York, pp 289–301
- [48] ASTM (2010) Standard test method for plastic strain ratio  $r$  for sheet metal, ASTM International, [www.astm.org](http://www.astm.org)
- [49] Yoon JI, Kim JG, Jung JM, Lee DJ, Jeong HJ, Shahbaz M, Lee S, Kim HS (2016) Obtaining reliable true plastic stress-strain curves in a wide range of strains using digital image correlation in tensile testing. *Korean J Met Mater* 54:231–236
- [50] ASTM (2013) Standard test method for measurement of fracture toughness, ASTM International, <http://www.astm.org>
- [51] Yoon JI, Jung J, Lee HH, Kim G-S, Kim HS (2016) Factors governing hole expansion ratio of steel sheets with smooth sheared edge. *Met Mater Int* 22:1009–1014
- [52] Hu W (2007) A novel quadratic yield model to describe the feature of multi-yield-surface of rolled sheet metals. *Int J Plast* 23:2004–2028
- [53] ABAQUS (2009) ABAQUS analysis user manual: version 6.9, Hibbit, Karlsson & Sorensen, Inc., Pawtucket, United States
- [54] Martinez-Paneda E, Garcia TE, Rodriguez C (2016) Fracture toughness characterization through notched small punch test specimen. *Mater Sci Eng A* 657:422–430
- [55] Hatanaka N, Yamaguchi K, Takakura N (2003) Finite element simulation of the shearing mechanism in the blanking of sheet metal. *J Mater Process Tech* 139:64–70
- [56] Oh CS, Kim NH, Kim YJ, Baek JH, Kim YP, Kim WS (2011) A finite element ductile failure simulation method using stress-modified fracture strain model. *Eng Frac Mech* 78:124–137
- [57] Bai Y, Wierzbicki T (2010) Application of extended Mohr-Coulomb criterion to ductile fracture. *Int J Fract* 161:1–20
- [58] Choi SH, Kim EY, Kim SI (2014) The micromechanical deformation behaviors of hot-rolled 590FB steel during hole-expansion test. *Int J Plast* 58:184–200